

Mapping of the Cold Neutral Medium via H I Phase Separation in an Atomic Cloud Undergoing Molecular Cloud Formation

Yamato MATSUZUKI,^{1,*} Hiroaki YAMAMOTO,¹ and Kengo TACHIHARA,¹

¹Department of Physics, Graduate School of Science, Nagoya University, Furo-cho, Chikusa-ku, Nagoya, Aichi 464-8602, Japan
*E-mail: y.matsuzuki@a.phys.nagoya-u.ac.jp

ORCID: 0009-0007-2537-3611, 0000-0001-5792-3074, 0000-0002-1411-5410

Abstract

We investigate the atomic-to-molecular gas transition in the molecular formation cloud HLCG 92–35. Using the ROHSA algorithm to decompose GALFA-H I data, we find the Lukewarm Neutral Medium (LNM) to be the dominant mass component, indicating a state driven out of thermal equilibrium by turbulence or past shocks. Spatial analysis reveals an inverse correlation between the phase distributions, with small-scale Cold Neutral Medium (CNM) structures embedded within an extended LNM envelope. Using Astrodendro, we identified 2,214 CNM clumps with sub-parsec scales. While the CNM mass spectrum steepens at high masses, its intermediate-mass slope matches that of CO clumps, suggesting that molecular clouds inherit the hierarchical structure of the CNM. Significant non-thermal linewidths and localized CNM-CO velocity offsets imply that the CNM consists of subsonic cloudlets moving collectively as aggregates. Our results show that these sub-parsec CNM structures are the fundamental building blocks of the cold interstellar medium, driven by thermal instability and turbulent compression.

Keywords: ISM: atoms — ISM: molecules — ISM: kinematics and dynamics — turbulence

1 Introduction

Star formation is a fundamental process driving the evolution of galaxies, and it originates in molecular clouds that form through the transition from neutral atomic hydrogen (H I) to molecular hydrogen (H₂). H I in the interstellar medium (ISM) is generally classified into three thermal phases: the high-temperature, low-density Warm Neutral Medium (WNM), the low-temperature, high-density Cold Neutral Medium (CNM), and the thermally unstable Lukewarm Neutral Medium (LNM), which occupies an intermediate regime between them (McClure-Griffiths et al. 2023). It is crucial to understand the physical processes that generate high-density, low-temperature structures, as this knowledge is key to revealing the mechanisms of molecular cloud formation and subsequent star formation. Therefore, it is essential to elucidate the multiphase structure of the H I gas and its evolution to understand the origins of star-forming regions.

The phase transition from H I to H₂ is expected to occur preferentially in denser and colder CNM. Numerous theoretical studies have explored the physical processes responsible for the formation of such CNM structures. Field (1965) and Field et al. (1969) first introduced the concept of thermal instability, establishing the theoretical foundation for the two-phase model of atomic gas, in which H I exists as a mixture of the WNM and the CNM. (Wolfire et al. 1995, 2003) conducted detailed thermal equilibrium calculations that incorporated the major heating and cooling processes in the ISM, thereby quantitatively defining the temperature and pressure structure of the two-phase neutral gas. More recent theoretical studies suggest that CNM structures can form via turbulent condensation within their precursor WNM (with temperatures of

~ 8,000 K and densities of ~ 0.3 cm⁻³). Numerical simulations (e.g., Hennebelle & Audit 2007; Saury et al. 2014) demonstrated that H I gas behaves as a turbulent, multiphase system in which CNM clumps with low volume-filling factors emerge as a consequence of local compressions in the WNM. The efficiency of CNM formation appears to depend on the properties of turbulence in the WNM (e.g., Seifried et al. 2011; Saury et al. 2014; Bellomi et al. 2020). Despite these advances, how H I gas, particularly the formation and evolution of CNM structures, sets the initial conditions for molecular cloud formation remains poorly understood.

Extensive H I absorption-line surveys have been conducted in the Milky Way in recent decades (e.g., Heiles & Troland 2003a, 2003b; Murray et al. 2015, 2018; Nguyen et al. 2024). These surveys provide increasingly detailed statistical descriptions of the H I phases, enabling investigations of the physical properties of atomic hydrogen in the interstellar medium. The spin temperature of the CNM is typically ~ 100 K, and the CNM accounts for roughly 30% of the total H I column density, with a significant fraction of thermally unstable gas also present. However, since absorption line studies rely on background continuum sources such as quasars, they probe only narrow lines of sight and cannot resolve the internal structure of CNM clouds on sub-parsec scales.

H I 21 cm emission line observations are essential for studying the spatial distribution of H I gas. Large-scale H I surveys of the Milky Way and nearby galaxies have been conducted (e.g., Kalberla et al. 2005; HI4PI Collaboration et al. 2016; Peek et al. 2018), and methods for quantifying the multiphase structure of H I emission have advanced considerably. Earlier attempts to distinguish WNM and CNM components relied on Gaussian decomposition based on line width differences (e.g., Kulkarni &

Fich 1985; Verschuur 1995), but the CNM component was often blended with WNM emission, making robust decomposition difficult. More recently, semi-automated Gaussian decomposition has been applied to large-area surveys to derive H I phase fractions (Haud & Kalberla 2007; Kalberla & Haud 2018). ROHSA, introduced by Marchal et al. (2019), performs regularized multi-Gaussian decomposition by exploiting spatial coherence between adjacent lines of sight, and it has become a powerful method for reconstructing consistent WNM and CNM distributions across wide fields of view (e.g., Marchal et al. 2021; Marchal & Miville-Deschênes 2021; Buckland-Willis et al. 2025).

Molecular clouds at high galactic latitude are ideal laboratories for studying molecular cloud formation. Located at $|b| > 20^\circ$, these clouds are expected to lie a few hundred parsecs from the Sun, given that the CO gas scale height of the Galactic disk is ~ 100 pc (Dame et al. 1987). They have relatively few overlapping background structures, simplifying the analysis. Furthermore, they are generally diffuse, and are often considered to represent early evolutionary stages in the transition from H I clouds to CO-bright molecular clouds.

HLCG 92–35, discovered by Yamamoto et al. (2003), is located at $(l, b) = (92^\circ, -35^\circ)$, and forms part of the high latitude molecular cloud complex MBM 53, 54, 55 (Magnani et al. 1985). In HLCG 92–35 region, H I gas is abundant near the center, while CO-emitting molecular clouds are concentrated toward the western portion. The total molecular mass in this western area is $\sim 330 M_\odot$. The far-infrared excess relative to the H I column density is the largest in the observed region, suggesting the presence of CO-poor H₂ gas. In addition, the ratio of far-infrared excess luminosity to H₂ mass is enhanced by a factor of about five compared to the surrounding MBM clouds, indicating that molecular gas is still in the process of forming. These characteristics therefore suggest that HLCG 92–35 represents an early evolutionary stage of molecular cloud formation. The MBM 53–55 complex is thought to be part of an evolved supernova remnant, and the H I gas is reported that the H I gas is expanding at a velocity of about 18 km s^{-1} (Gir et al. 1994). This dynamical environment provides a plausible source of external compression, and the morphology of HLCG 92–35 is consistent with a scenario in which a shock wave from the west has recently triggered molecular cloud formation. Because this region lies at a Galactic latitude of -35° , confusion with unrelated line-of-sight structures is relatively low, enabling a clearer assessment of its early-stage properties.

In this study, we investigate the spatial distribution of H I phases and CNM clump structures in the high-latitude molecular cloud HLCG 92–35 to observationally elucidate the evolutionary process from the atomic to the molecular phase. We apply the multi-Gaussian decomposition method ROHSA to high-resolution H I data of the HLCG 92–35 region. By analyzing the phase separation of H I components, we aim to reveal how atomic gas evolves into molecular clouds. The structure of this paper is as follows. Section 2 describes the H I and CO data used in this study. Section 3 outlines the multi-Gaussian decomposition method ROHSA and the model selection process. Section 4 presents the results of the H I component separation in the HLCG 92–35 region. Section 5 discusses the spatial distributions and physical properties of the identified H I phases and their implications for the molecular cloud formation process.

2 Data

Figure 1(a) and (b) show the integrated intensity maps of H I and ¹²CO ($J = 1-0$) emission toward the HLCG 92–35 region. The distance to the MBM 53, 54, 55 complex, which encompasses HLCG 92–35, was estimated to be ~ 150 pc by Welty et al. (1989) based on stellar Na I absorption measurements. In this study, we adopt a distance of 150 pc for this region.

2.1 H I data

The H I data used in this study are taken from the GALFA-H I Data Release 2 (DR2) archive (Peek et al. 2018). The observations were carried out with the 305 m Arecibo radio telescope, providing an angular resolution of $4'$ on a $1'$ grid. At a distance of 150 pc (the assumed distance to HLCG 92–35), this corresponds to a spatial resolution of ~ 0.18 pc. The velocity resolution is 0.184 km s^{-1} , which is sufficient to resolve the narrow spectral features characteristic of the CNM.

Details of the GALFA-H I survey observations and data reduction procedures are described in Peek et al. (2018). The analyzed field is shown in Figure 1(a). The data cube was trimmed to a velocity range of $-95.5 \leq v_{\text{LSR}} \leq 69.1 \text{ km s}^{-1}$, resulting in a data size of $350 \times 500 \times 900$ voxels (height \times width \times velocity channels). The H I emission is mainly concentrated in the range $-20 \leq v_{\text{LSR}} \leq 10 \text{ km s}^{-1}$, with no significant intermediate- or high-velocity components detected.

2.2 CO data

We used ¹²CO ($J = 1-0$) data obtained with the NANTEN 4 m radio telescope to trace the molecular cloud. The survey covers an area of $\sim 141 \text{ deg}^2$ within the Galactic coordinates $82^\circ \leq l_{\text{LSR}} \leq 98^\circ$ and $-45^\circ \leq b \leq -29^\circ$, encompassing the MBM 53, 54, and 55 complex. In this study, we utilized the portion of the dataset corresponding to the vicinity of HLCG 92–35.

The initial observations were carried out on a grid spacing of $8' \cos b$ in Galactic longitude and $8'$ in Galactic latitude. Regions exhibiting significant ¹²CO ($J = 1-0$) emission were subsequently re-observed at a finer spacing of $4' \cos b$ and $4'$, respectively. The angular resolution of the telescope was $\sim 2'.6$, the velocity resolution was 0.10 km s^{-1} , and the typical rms noise level was about 0.5 K per channel. The observed velocity range was $-25 \leq v_{\text{LSR}} \leq 10 \text{ km s}^{-1}$, consistent with the velocities of the main H I emission components. Details of the observations and data reduction are given in Yamamoto et al. (2003).

To ensure spatial consistency between the H I and CO datasets, the CO data cube was cropped to match the H I field and analyzed over the same area. The analyzed CO region is shown in Figure 1(b).

3 H I spectral decomposition method

To decompose the H I spectra, we employed the multi-Gaussian decomposition algorithm ROHSA (Regularized Optimization for Hyper-Spectral Analysis; Marchal et al. 2019). ROHSA performs spectral decomposition by fitting a linear combination of Gaussian functions to the observed H I profiles. The fitted model T_{model} is expressed as the sum of multiple Gaussian components:

$$T_{\text{model}}(\mathbf{r}, v_z) = \sum_{i=1}^N G_i(\mathbf{r}, v_z) \quad (1)$$

where each Gaussian component at position \mathbf{r} and line-of-sight velocity v_z is defined as

$$G_i(\mathbf{r}, v_z) = a_i(\mathbf{r}) \exp\left(-\frac{(v_z(\mathbf{r}) - \mu_i(\mathbf{r}))^2}{2\sigma_i^2(\mathbf{r})}\right) \quad (2)$$

where $a_i(\mathbf{r})$, $\mu_i(\mathbf{r})$, and $\sigma_i(\mathbf{r})$ represent the amplitude (= peak brightness temperature), central velocity, and velocity dispersion of the i -th Gaussian component, respectively.

In general, increasing the number of Gaussian components N reduces the residuals and improves the fit to the observed spectra. However, using an excessively large number of components may result in overfitting to noise and does not necessarily yield a physically meaningful decomposition. To mitigate this, ROHSA adopts a regularized nonlinear least-squares approach that enforces spatial coherence among neighboring pixels.

This regularization allows for a consistent decomposition even in complex lines of sight where multiple components with different spatial distributions and central velocities overlap. Furthermore, ROHSA performs the optimization in a multi-resolution framework, in which the fitting is carried out progressively from low to high spatial resolution. This hierarchical approach ensures that both large-scale and small-scale structures are properly captured in the final model.

3.1 ROHSA parameters

In the Gaussian decomposition with ROHSA, it is necessary to specify the number of Gaussian components used for the decomposition, n_{gauss} , as well as the strengths of the regularization terms λ_a , λ_μ , λ_σ , and λ'_σ (see Marchal et al. 2019 for details of these parameters). These parameters must be optimized for each dataset individually. ROHSA allows the amplitude of a Gaussian component to be set to zero during the fitting process. Therefore, n_{gauss} represents the maximum number of Gaussian functions used for the decomposition, and it does not necessarily mean that all spectra in the region are fitted with exactly n_{gauss} components.

To evaluate how accurately the model derived by ROHSA reproduces the observed data, we introduced the ratio of the noise RMS to the residual RMS (hereafter referred to as the r.m.s. ratio), defined as (noise RMS)/(residual RMS).

This quantity compares the noise level in the observed data with that in the residual data of the model: values close to unity indicate that the ROHSA model reproduces the data with high fidelity.

The noise RMS was calculated from emission-free regions (pixels 500–650 and 1350–1400), while the residual RMS was derived from the residuals in the emission-dominated region (pixels 650–1350).

4 Result

4.1 Model selection

Table 1 summarizes the results for a total of 60 parameter combinations. The indicator shown is the r.m.s. ratio (noise RMS / residual RMS). Previous studies (e.g., Taank et al. 2022) were set to have the same value of the parameters ($\lambda_a, \lambda_\mu, \lambda_\sigma$) to enable efficient parameter exploration.

The r.m.s. ratio ranges from 0.64 to 0.92, exhibiting a general trend that it approaches unity as the number of Gaussian components N increases and the constraint term λ'_σ decreases. However, when N becomes excessively large, the r.m.s. ratio tends to decrease again. While increasing N allows the model to reproduce more complex spectral structures, it can also weaken the spatial

regularization and the coherence among adjacent pixels, occasionally leading to a local degradation of the fitting accuracy. The fact that the r.m.s. ratio remains below unity for all fittings indicates that the residuals of the model exceed the observational noise level. This is likely due to limitations in spatial resolution, which prevent a complete reproduction of the observed spectra using a simple sum of Gaussian components, as well as to the presence of small residual structures such as baseline variations that are not captured by the model. Among the tested combinations, the parameter set $(N, \lambda_a, \lambda_\mu, \lambda_\sigma, \lambda'_\sigma) = (9, 10, 10, 10, 1)$ yielded the best performance and was therefore adopted for the subsequent analysis.

Figure 2 (top) shows a scatter plot of all Gaussian components obtained using the selected parameter set $(N, \lambda_a, \lambda_\mu, \lambda_\sigma, \lambda'_\sigma) = (9, 10, 10, 10, 1)$. The horizontal axis represents the full width at half maximum (FWHM = $2\sqrt{2\ln 2}\sigma$, where σ is the velocity dispersion), and the vertical axis indicates the peak intensity. In total, 1,575,000 Gaussian components corresponding to all fitted spectra are plotted, including those with zero amplitude as allowed by ROHSA. The components are distributed over a range of ~ 1 –15 km s⁻¹ in FWHM and up to ~ 30 K in peak intensity. The plot reveals three distinct clusters in the peak intensity–velocity dispersion plane. The mean parameter values for each Gaussian component are summarized in Table 2. Based on these values, we define the components with the smallest mean velocity dispersions (G_2, G_3, G_4, G_5, G_6 , and G_8) as CNM, those with the largest dispersions (G_7 and G_9) as WNM, and the intermediate component (G_1) as LNM.

Figure 2 (top) shows the distribution of Gaussian components in the FWHM–peak intensity plane for the CNM, LNM, and WNM phases. Figure 2 (bottom) presents the histogram of FWHM values for the Gaussian components associated with each phase. While the phase separation is generally clear, a slight overlap is observed between the CNM and LNM populations, as well as marginal overlap among the CNM, LNM, and WNM components. Examples of the spectral fitting results are shown in Figure 3. The observed H I spectra are plotted in gray, and the best-fit profiles obtained with ROHSA are shown in green. The individual Gaussian components corresponding to the CNM, LNM, and WNM phases are indicated by blue, purple, and red curves, respectively, consistent with the phase definitions in Figure 2.

4.2 Column density maps

Figure 4 shows the spatial distributions of the column densities for the CNM, LNM, and WNM components defined in the previous section. The column density was calculated from the brightness temperature $T_B(v)$ and velocity width dv of the spectrum using the following equation:

$$N_{\text{HI}} = 1.822 \times 10^{18} \int T_B(v) dv \quad [\text{cm}^{-2}] \quad (3)$$

This calculation assumes that the H I gas is optically thin ($\tau \ll 1$). The total H I mass is given by

$$M_{\text{HI}} = \sum m_{\text{H}} N_{\text{HI}} \times S \quad [M_\odot] \quad (4)$$

where m_{H} is the mass of a hydrogen atom (1.6737×10^{-27} kg) and S is the projected area of each pixel.

If the H I gas is optically thick, the column density should instead be estimated as

$$N_{\text{thick, HI}} = 1.822 \times 10^{18} \int \frac{\tau(v) T_B(v)}{(1 - e^{-\tau(v)})} dv \quad [\text{cm}^{-2}] \quad (5)$$

for which N_{HI} remains below $N_{\text{thick,HI}}$.

However, correcting for optical depth effects requires knowledge of both the spin temperature and the optical depth, which cannot be obtained from emission-line observations alone.

However, accurate correction for optical-depth effects necessitates independent estimates of both the spin temperature and the optical depth, which cannot be constrained by emission-line data alone. To date, the optically thick column density $N_{\text{thick,HI}}$ has been derived from combined on–off spectra toward radio continuum background sources, and the corresponding statistical correction factor $f = N_{\text{thick,HI}}/N_{\text{HI}}$ has been investigated. Although this correction factor varies among different regions, observations at high Galactic latitudes suggest that for column densities of $\sim 10^{20} \text{ cm}^{-2}$, f is close to unity, and even at $\sim 10^{21} \text{ cm}^{-2}$, $f \sim 1.3$ (e.g., Lee et al. 2015; Nguyen et al. 2019, 2024). Even if the column densities derived in this work are underestimated by up to $\sim 30\%$, the resulting uncertainty is not large enough to change the results at the order-of-magnitude.

The spatial distributions reveal that both the CNM and LNM exhibit intricate and filamentary substructures, with the CNM showing particularly fine-scale morphology. For instance, around $(l, b) \sim (94.5^\circ, -36.5^\circ)$ and $(92.9^\circ, -36.4^\circ)$, small clumpy CNM features are seen to be surrounded by more diffuse LNM structures. Such clumpy CNM structures are found at multiple locations across the region. Typically, CNM structures have characteristic sizes of $\lesssim 1 \text{ pc}$, while LNM structures tend to be comparable or somewhat larger in scale. The tendency for LNM to envelop CNM features is consistent with the all-sky phase separation reported by Kalberla & Haud (2018), as well as with numerical simulations showing that LNM preferentially forms around CNM regions and along sheet-like structures surrounding dense condensations (e.g., Gazol & Kim 2001; Saury et al. 2014). In contrast, the WNM exhibits a more diffuse morphology with a broader and smoother spatial distribution compared to the other two phases.

Assuming optically thin conditions, the total H I mass of HLCG 92–35 is estimated to be $\sim 2200 M_\odot$, of which the CNM, LNM, and WNM contribute $946 M_\odot$, $1034 M_\odot$, and $220 M_\odot$, respectively. The resulting mass fractions are CNM : LNM : WNM = 43 : 47 : 10. The WNM thus accounts for only about 10% of the total mass, whereas the thermally unstable LNM comprises nearly half. This result indicates that, in the HLCG 92–35 region, a substantial fraction of the warm H I gas exists in the thermally unstable phase.

5 Discussion

5.1 Spatial correlation among H I phases

Figure 5 presents the two-dimensional frequency distributions of the mass fractions of each H I phase along the same line of sight. The mass fraction of the CNM is defined as $f_{\text{CNM}} = N_{\text{CNM}}/N_{\text{HI}}$, and those of the LNM and WNM are defined analogously. The diagonal distribution seen in Figure 5(a) indicates a strong anti-correlation between the CNM and LNM, suggesting that CNM-dominated and LNM-dominated regions are spatially complementary along the line of sight. This implies that relatively large-scale LNM structures contain smaller, compact CNM condensations embedded within them. In contrast, Figure 5(b) shows that the distributions of the WNM and CNM are more diffuse and exhibit only a weak positive correlation. This implies that the WNM occupies a larger-scale volume in which both LNM and CNM components are nested. Such a morphological relationship among the three phases is consistent with a scenario in which the WNM undergoes

thermal instability and subsequently fragments into smaller-scale structures. (e.g., Koyama & Inutsuka 2002).

Kalberla & Haud (2018) performed a similar two-dimensional frequency analysis using the all-sky HI4PI survey and found that, on average, the LNM dominates globally with $f_{\text{CNM}} \lesssim 0.15$, $f_{\text{LNM}} \sim 0.55$, and $f_{\text{WNM}} \sim 0.30$. However, in the local small-scale, filamentary components they identified, high f_{CNM} values and a strong CNM–LNM anti-correlation were observed, which are qualitatively consistent with Figure 5.

5.2 H I phase fraction

The mass ratio among the phases is CNM:LNM:WNM = 43:47:10, indicating that most of the H I in the HLCG 92–35 region resides in the LNM and CNM. The substantial fraction of the LNM is inconsistent with the simple thermal equilibrium picture predicted by the classical two-phase model McKee & Ostriker (1977). In a static thermal equilibrium model, the LNM is expected to disperse within $\approx 1 \text{ Myr}$. Therefore, the observed high LNM fraction implies that continuous external energy injection is operating, keeping the gas persistently out of thermal equilibrium.

Previous studies based on H I absorption line observations (e.g., Heiles & Troland 2003b; Roy et al. 2013b; Murray et al. 2015, 2018) have reported that, near the Galactic plane, $\sim 30\%$ of the H I is the CNM, and $\sim 20\%$ to the LNM. In contrast, more localized observations have revealed large regional variations in the H I phase fractions: in the NEP region, CNM $\approx 8\%$, LNM $\approx 28\%$, and WNM $\approx 64\%$ (Marchal & Miville-Deschênes 2021), whereas in the NCPL, Taank et al. (2022) find CNM $\approx 50\%$, LNM $\approx 21\%$, and WNM $\approx 27\%$ for the LVC on loop (noting that the sum does not reach 100% because only the LVC is considered). Compared with these, the H I phase fractions derived in this study show that the CNM is somewhat dominant, while the unstable LNM accounts for nearly half of the total mass. The fact that the WNM constitutes only about 10% of the total suggests that the phase transition toward the CNM is already in progress and that the external supply of WNM is limited. Moreover, the presence of such a large fraction of LNM indicates that the region cannot be explained by a simple thermal equilibrium state. This implies an environment where dynamical or turbulent energy continuously perturbs the thermal balance.

The presence of large amounts of LNM is consistent with theoretical predictions (Audit & Hennebelle 2005; Hennebelle & Audit 2007; Kim & Ostriker 2018) that turbulence driven by external energy injection continuously drives the H I gas out of thermal equilibrium, confining a significant fraction of it within thermally unstable regimes. Indeed, numerical simulations demonstrate that increasing the intensity of turbulence enhances the LNM mass fraction, reaching 40–50% of the total H I mass (Kobayashi et al. 2020; Seifried et al. 2020a, 2020b; Hu 2025). The high LNM fraction derived in this study is consistent with these findings and suggests that turbulence is actively operating in the observed region. Furthermore, since gas in the thermally unstable phase is expected to evolve into the CNM within a few Myr (e.g., Inoue & Inutsuka 2012), the LNM \rightarrow CNM phase transition is likely still ongoing in this region.

The MBM 53, 54, and 55 complex, which encompasses the HLCG 92–35 region, is believed to have formed as a consequence of shock waves from a past supernova explosion (Gir et al. 1994), and an expanding H I shell structure is still observed there. These characteristics suggest that turbulence is being sustained by the injection of kinetic energy from past shock events,

providing physical conditions capable of maintaining a high LNM fraction. Therefore, the prominent presence of thermally unstable gas in this region serves as an important observational signature that the thermal and dynamical state of the H I is still strongly influenced by dynamical perturbations induced by previous shock-driven processes.

5.3 Physical properties of CNM and CO clumps

5.3.1 Identifying clumps: Astrodendro

To identify clumpy structures, we employed the Python package Astrodendro, which implements the dendrogram-based analysis method described by Rosolowsky et al. (2008). This approach was adopted because CNM structures associated with the H I phase transition exhibit inherently multiscale morphology. In our analysis, Astrodendro was applied to the integrated intensity maps of each CNM component to identify leaf structures. The use of integrated intensity maps enables the detection of structures characterized by high spectral intensity. Since Astrodendro are data-driven algorithms and most of the CNM integrated intensities satisfy the 5σ detection threshold adopted in this study as described below, the influence of parameter selection on the results is expected to be limited (Goodman et al. 2009; Marchal et al. 2021).

5.3.2 Derivation of Physical Properties

To prevent the extraction of spurious structures caused by noise during clump identification, the following parameters were adopted in Astrodendro.

First, the minimum intensity required for a structure to be identified was set to `min_value` = 3.56, corresponding to the 5σ detection limit in the integrated intensity map of the GALFA-H I dataset. Structures below this threshold were excluded from the analysis. In addition, to ensure that a structure is identified as an independent leaf separated from neighboring structures, its peak intensity was required to exceed the merge level with adjacent structures by at least `min_delta` = 3.56. Furthermore, to guarantee that each identified leaf has sufficient spatial extent, we adopted `min_npix` = 16. Given the $1'$ sampling interval and the effective beam size of $\sim 4'$ in the GALFA-HI data, one beam corresponds to roughly 16 pixels. This criterion prevents small-scale fluctuations significantly smaller than the beam size from being mistakenly identified as leaves.

For each identified clump, we derived its size (diameter), mass, and mean density.

The clump size was defined from the area A occupied by the identified leaf as the diameter of a circle with the same area, $L = 2\sqrt{A/\pi}$.

The clump mass M_{CNM} was calculated as

$$M_{\text{CNM}} = m_{\text{H}} \sum [d^2 \Omega N(\text{CNM})] \quad (6)$$

where m_{H} is the mass of a hydrogen atom, d is the distance to the cloud, Ω is the solid angle per pixel ($1'$), and $N(\text{CNM})$ is the column density of the CNM within the region occupied by the leaf structure. The Σ on the right-hand side represents the sum over all pixels comprising the clump. Assuming the gas is optically thin, $N(\text{CNM})$ was derived using Equation (3).

The mean number density of each clump was then estimated from its mass M_{CNM} and diameter L . As before, this estimate should be regarded as a lower limit.

$$n_{\text{CNM}} = M_{\text{CNM}} / [(4/3)\pi(L/2)^3] [\text{cm}^{-3}] \quad (7)$$

A dendrogram analysis was also performed on the ^{12}CO ($J=1-0$) integrated intensity map of the HLCG 92–35 region using Astrodendro. The adopted parameters were `min_value` = 0.9 ($\approx 3\sigma$), `min_delta` = 0.6 ($\approx 2\sigma$), and `min_npix` = 2. Structures with at least two pixels were identified as clumps. The clump mass was calculated as

$$M_{12\text{CO}} = \mu m_{\text{H}} \int [d^2 \Omega N(\text{H}_2)] dS \quad (8)$$

where m_{H} is the mass of a hydrogen atom, d is the distance to the cloud, and Ω is the solid angle per pixel ($4'$). The molecular hydrogen column density, $N(\text{H}_2)$, was derived from the integrated intensity of ^{12}CO using a CO-to- H_2 conversion factor of $1.3 \times 10^{20} \text{ cm}^{-2} / (\text{K km s}^{-1})$ as measured for high-latitude molecular clouds Cotten & Magnani (2013). The mean molecular weight per hydrogen molecule, μ , was taken to be 2.0. (For comparison, Yamamoto et al. 2003 assumed a 25% helium content in molecular clouds and adopted $\mu = 2.8$.)

5.3.3 Physical properties of CNM clumps

A total of 2,214 CNM clumps were identified. Many of these clumps overlap along the line of sight and therefore cannot be clearly separated in the integrated intensity maps shown in Figures 1 and 4.

Figure 6(a) shows the diameter distribution of the CNM clumps, which ranges from 0.2 to 2.3 pc, close to the spatial resolution limit of the data, with an average diameter of 0.4 ± 0.2 pc. Only 38 clumps (1.7%) have diameters larger than 1 pc. This result indicates that most CNM structures visible in the integrated intensity map, which appear to extend over several parsecs, are in fact composed of multiple smaller, clump-like substructures.

Although the present study is still affected by spatial resolution limitations, its spatial resolution is improved relative to previous studies (e.g., Marchal et al. 2019), allowing us to probe CNM structures on smaller scales. The results of the present study clearly demonstrate that the CNM is composed of fine structures on sub-parsec scales when observed with higher spatial resolution. Theoretical simulations by Kobayashi et al. (2023) have shown CNM clump sizes ranging from 0.03 to several pc, peaking around 0.1 pc. The size distribution obtained in this study is consistent with these theoretical predictions, supporting the interpretation that the CNM is characterized by sub-parsec-scale clumpy structures.

Figure 6(b) shows the number density distribution of the CNM clumps. The derived densities range from 4 cm^{-3} to 560 cm^{-3} , with an average value of $102 \pm 82 \text{ cm}^{-3}$. This result is in good agreement with the mean CNM number density of 76 cm^{-3} estimated by Kalberla et al. (2025) for high galactic latitude regions based on absorption line observations. This indicates that our results are consistent with those derived from absorption data. High-density CNM clumps are considered potential sites for the onset of molecular cloud formation. As shown in Figure 6(b), clumps with densities below 100 cm^{-3} constitute the majority, while only 271 clumps (12% of the total) have densities above 200 cm^{-3} . As the CNM becomes denser, molecular hydrogen is expected to form within the clumps, suggesting that the CNM density tends to saturate at several hundred cm^{-3} . Indeed, numerical simulations of H_2 formation by Valdivia et al. (2016) demonstrate that most H_2 molecules form at densities of a few hundred cm^{-3} . Consequently, the CNM density is expected to reach a natural plateau as the gas transitions into the molecular phase. Other theoretical simulation

studies (e.g., Fukui et al. 2018) have also shown that the maximum CNM density reaches 10^3 cm^{-3} . The spatial resolution of the simulations in Fukui et al. (2018) was 0.02 pc, whereas the observational data used in this study are affected by beam dilution. Consequently, the maximum CNM densities derived here are expected to be slightly lower than the simulation values, however generally fall within the upper end of the 10^2 cm^{-3} range.

5.3.4 Mass spectrum of CNM clump and CO clump

The derived CNM clump mass spectrum is shown in Figure 7(a). The masses of the CNM clumps range from $3.0 \times 10^{-3} M_\odot$ to $1.4 M_\odot$. The detection limit of N_{HI} in the GALFA–HI DR2 data is $\approx 6.5 \times 10^{18} \text{ cm}^{-2}$ (Peek et al. 2018), which corresponds to a mass detection threshold of $\approx 1.59 \times 10^{-3} M_\odot$ derived using Astrodendro. The mass distribution of the clumps, expressed as the number per unit mass $dN/dM \propto M^{-\gamma}$, follows a power-law form with $\gamma = 1.92 \pm 0.08$ for clump masses in the range of $0.05 < M < 0.5 M_\odot$ and $\gamma = 4.19 \pm 0.85$ for $M > 0.5 M_\odot$. The high-mass end of the distribution is subject to large uncertainties owing to the small number of detected clumps.

The spectral slope obtained for the intermediate-mass range is in good agreement with values reported in simulations of WNM inflows (e.g., Heitsch et al. 2005; Hennebelle & Audit 2007; Inoue & Inutsuka 2012; Kobayashi et al. 2023). Hennebelle & Audit (2007) investigated the cooling of turbulent H I gas flows using two-dimensional simulations and demonstrated that CNM clumps formed via thermal instability exhibit hierarchical and statistically self-similar structures. Using an analytical approach based on Press–Schechter theory, they showed that if the spectrum of initial density fluctuation has an exponent of $n = 11/3$ (Kolmogorov type), the resulting mass distribution of clumps formed through thermal instability follows $\gamma = 2 - (n - 3)/3 \simeq 1.8$. The close agreement between the spectral index derived in this study and this theoretical prediction indicates that the intermediate-mass CNM clumps were produced during the growth of density structures driven by thermal instability.

Figure 7(b) shows the mass distribution of CO clumps in the HLCG 92–35 region identified in Section 5.3.2. The red points denote the CO clump mass spectrum, while the blue vertical line indicates the position of the break in the CNM clump mass spectrum at $0.5 M_\odot$. The masses of the CO clumps range from 0.16 to $24 M_\odot$. The 3σ detection limit for the H_2 column density is $1.2 \times 10^{20} \text{ cm}^{-2}$, corresponding to a mass detection limit of $\sim 0.12 M_\odot$ (red dashed line in the figure). The CO clump mass distribution follows a single power law, $dN/dM \propto M^{-1.86 \pm 0.06}$, for $M > 0.5 M_\odot$. This slope is comparable to that found in the intermediate-mass range of CNM clumps. This similarity suggests that molecular clouds may form while inheriting the mass distribution of CNM structures.

The steepening of the mass distribution in the range $M \gtrsim 0.5 M_\odot$ may reflect the evolutionary stage of massive CNM clumps transitioning into molecular clouds. As these massive CNM clumps grow, their internal densities increase, promoting the formation of H_2 . As H_2 formation proceeds, the fraction of mass contained in atomic hydrogen decreases over time, leading to a sharp decline in the number of massive clumps remaining within the CNM regime. Consequently, the steepening of the mass spectrum can be interpreted as a statistical signature of the ongoing transition from CNM to H_2 . Indeed, massive clumps are generally denser, and the rate coefficient for H_2 formation on dust grain surfaces is known to increase rapidly with the density of atomic hydrogen (Tielens & Hollenbach 1985). Therefore, mas-

sive and dense CNM clumps are expected to evolve into molecular clouds on relatively short timescales, resulting in a decrease in the mass observed as CNM. Supporting this interpretation, Valdivia et al. (2016) analyzed simulations of molecular cloud formation in which clumps were identified based on the total hydrogen number density ($n = n_{\text{CNM}} + 2n_{\text{H}_2}$) and the molecular hydrogen fraction, $f(\text{H}_2) = 2n_{\text{H}_2}/n_{\text{CNM}}$, within each clump was statistically evaluated. They found that clumps with masses of $\sim 0.1 M_\odot$ already exhibit $f(\text{H}_2) > 0.2$, while more massive clumps with $M \gtrsim 1 M_\odot$ typically reach $f(\text{H}_2) \gtrsim 0.8$. This demonstrates a systematic increase of the molecular fraction with increasing clump mass. Note, however, that the clumps in their study were defined using a relatively high density threshold of $n = 1000 \text{ cm}^{-3}$. Even for clumps with $f(\text{H}_2) \gtrsim 0.8$, this corresponds to $n_{\text{CNM}} \gtrsim 200 \text{ cm}^{-3}$, and the analysis therefore focuses on comparatively dense clumps.

On the other hand, the Astrodendro analysis itself may contribute to an underestimation of the number of massive clumps. Specifically, the choice of the parameter `min_delta` could cause small noise-induced substructures to be identified as independent clumps, thereby artificially lowering the count of massive ones. However, the overall trend in the mass distribution remains consistent even when `min_delta` is varied, suggesting that the influence of such analysis biases is likely limited.

The fact that intermediate-mass CNM clumps and CO clumps follow the same power-law distribution suggests that the hierarchical density structures generated by thermal instability and turbulent compression are inherited from the CNM to the CO phase. The self-similarity in the mass distribution appears to be established during the formation of CNM from the WNM and to be preserved into the molecular cloud stage. This result indicates that thermal instability consistently produces hierarchical structures from the CNM to molecular clouds, with only minor contributions from H I heating/cooling processes and the H I-to- H_2 transition.

Deviations from the power-law at the low-mass end ($M \lesssim 0.05 M_\odot$) are likely caused by the limited spatial resolution of the observations. In three-dimensional simulations by Inoue & Inutsuka (2012) and Kobayashi et al. (2023), the mass function continues to follow a power-law even below $0.05 M_\odot$. In contrast, the present study shows clear deviations in this low-mass regime, indicating a relative deficiency of low-mass CNM clumps (i.e., smaller-sized structures) compared with the simulations. This discrepancy suggests that low-mass clumps may be missed observationally or that multiple unresolved clumps are blended into a single detected structure. Audit & Hennebelle (2010) examined clump masses at various spatial resolutions and found that the lower-mass turnover from the power law shifts to smaller masses as resolution improves. The spatial resolution of their simulations ($\sim 0.02 \text{ pc}$) is about an order of magnitude finer than that of the GALFA–HI data used in this study ($\sim 0.2 \text{ pc}$). Numerical simulations predict that numerous low-mass CNM clumps exist on sub-0.1 pc scales, which fall below the resolution limit of the current observations. Consequently, these small clumps are likely unresolved or undetected in our data. Therefore, the apparent deficiency of low-mass clumps arises primarily from observational limitations and is expected to be mitigated by future H I observations with higher angular resolution.

5.4 Velocity dispersion of the CNM spectrum

The line width of the separated CNM components is generally broader than the thermal line width expected from the canonical

CNM temperature. The spectral velocity dispersion, σ , is related to the gas kinetic temperature, T_k , by

$$T_k = \frac{\sigma^2 m_H}{8k_B \ln 2} \simeq 21.855 \Delta V_{\text{FWHM}}^2 \simeq 3.9\sigma^2 \quad (9)$$

where ΔV_{FWHM} is the full width at half maximum in km s^{-1} . For reference, the thermal velocity dispersion of H I gas at 100 K is $\sim 0.91 \text{ km s}^{-1}$.

The observed velocity dispersion includes both thermal and nonthermal contributions. The total dispersion, σ_{obs} , can be expressed as

$$\sigma_{\text{obs}}^2 = \sigma_{\text{th}}^2 + \sigma_{\text{nt}}^2 = \frac{k_B T_k}{m_H} + \sigma_{\text{nt}}^2 \quad (10)$$

where σ_{th} and σ_{nt} denote the thermal and nonthermal velocity dispersions, respectively.

Extensive H I absorption-line observations have enabled direct measurements of the CNM spin temperature. For example, the BIGHICAT catalog, which compiles Galactic H I absorption-line data, contains 1370 detected CNM components and shows that the CNM spin temperature distribution peaks in the range of 50–200 K (McClure-Griffiths et al. 2023). Only a small fraction of components exhibit higher temperatures: 5.0% exceed 500 K, and 1.7% exceed 1000 K. Owing to the high density of the CNM, frequent collisions with electrons, ions, and hydrogen atoms drive the hyperfine level populations of the 21 cm line toward thermal equilibrium. Consequently, the spin temperature, T_s , is expected to be approximately equal to the kinetic temperature, T_k , allowing a direct comparison between the two.

Figure 8 presents the distributions of spin temperature T_s and Doppler temperature T_D derived from BIGHICAT. The Doppler temperature is calculated from the observed H I velocity dispersion σ_{obs} via $T_D \simeq 3.9\sigma_{\text{obs}}^2$. Components with $T_s < 250$ K are classified as CNM, and are indicated by blue points. A general trend of $T_D > T_s$ is apparent, implying that the observed CNM line widths cannot be attributed solely to thermal motion and that non thermal velocity dispersion contributes significantly. Defining the Mach number as $M_t = 4.2(T_D/T_s - 1)$, a fit to the distribution yields $M_t \simeq 4.6$, indicating that many CNM components are in a strongly supersonic regime. Consequently, CNM generally exhibits line widths considerably broader than expected from thermal motion alone, consistent with supersonic internal motions.

Figure 9 shows the distribution of line widths, expressed as equivalent temperatures, for all CNM components decomposed by ROHSA. The upper axis converts line width to temperature. The temperatures inferred from CNM line widths range from 0 to 2,500 K, with most components concentrated below 1,200 K. A prominent peak appears around 300 K, and the mean value is ~ 530 K. This is significantly higher than the typical CNM temperatures suggested by simulations or absorption-line measurements, indicating that the line-width-derived temperatures are not purely thermal in origin but include a substantial contribution from non-thermal velocity dispersion, consistent with the absorption-line results.

Several studies have investigated the velocity dispersion of CNM components. For instance, Marchal et al. (2021) derived CNM temperatures from velocity dispersion using a method similar to that employed in this work. However, their reported mean value of $1.6 \pm 1.1 \text{ km s}^{-1}$ is comparable to their data's spectral resolution of 1.32 km s^{-1} , suggesting that their results were likely affected by instrumental limitations. In contrast, the GALFA-H I data used in this study provide a much higher spectral resolution

of 0.184 km s^{-1} , sufficient to resolve thermal line widths corresponding to gas temperatures below 100 K. Therefore, uncertainties due to instrumental resolution are expected to be minimal in the present analysis.

In addition, the 21 cm line exhibits a relatively broad line width, as the hydrogen atom has a much smaller mass than most other atoms and molecules (e.g., H is 1/28 the mass of CO). Consequently, when multiple CNM components exist along the line of sight with similar radial velocities, their spectral features can overlap, making it difficult to separate individual components. Moreover, because atomic hydrogen is more spatially extended and abundant than molecular gas, multiple overlapping components are more likely to occur, introducing additional uncertainty into the observed velocity dispersion.

5.5 Central velocity offset between CO and CNM

Figure 10 presents the cumulative distribution of the central velocity difference between the $^{12}\text{CO}(J=1-0)$ emission line and the CNM components. Because multiple CNM components can exist along the same line of sight, the velocity offset was calculated between each CO emission line and the CNM component whose central velocity was closest to that of the CO line. Only pixels with CO peak intensities above 0.2 K were included in the analysis. The results indicate that the two components are not perfectly coincident in velocity. Offsets exceeding 0.5 km s^{-1} were found in $\sim 40\%$ of the components, while offsets greater than 1.0 km s^{-1} occurred in about 10%.

Figure 11 shows representative example of velocity offsets between CNM and CO. The blue spectra correspond to CNM (dashed lines indicate all CNM components), and the gray spectra correspond to CO. Each spectrum was fitted with a Gaussian function; poorly fitted cases were excluded, and for CO spectra with multiple peaks, only the strongest component was considered.

Park et al. (2023) also reported velocity offsets between CO and CNM along several lines of sight based on H I absorption observations toward 58 positions across the sky. Their analysis revealed velocity differences ranging from 0.01 to 4.3 km s^{-1} , with a median of 0.4 km s^{-1} . Furthermore, a velocity difference of $0.06\text{--}2.64 \text{ km s}^{-1}$ (median 0.5 km s^{-1}) was also found between CNM and OH absorption components. Possible large-scale kinematic origins of the observed velocity offsets, such as Galactic rotation or expansion motions, were considered. In contrast to absorption-line studies limited to individual line of sights, the present spatially resolved analysis enables an examination of the spatial distribution of these velocity offsets. However, no systematic trend was found in their direction or spatial distribution. This result indicates that the observed displacements are primarily associated with local phenomena rather than global kinematic effects. These results suggest that, if molecular clouds form within dense regions embedded in CNM cores, only a portion of the CNM along a given line of sight contributes to molecular cloud formation. In other words, the CNM component observed along a single line of sight likely consists of multiple unresolved, small-scale CNM substructures, not all of which are directly involved in the formation of molecular clouds. Rather, molecular cloud evolution is thought to proceed only within those CNM regions that satisfy specific physical conditions such as sufficient density, shielding, and pressure balance.

5.6 Interpretation of the CNM line broadening

The CNM line broadening discussed in Section 5.4, together with the velocity offsets between CO and CNM discussed in Section 5.5, suggests the presence of internal substructure within the CNM. In this section, we discuss the possibility that the non-thermal contribution to the CNM linewidth originates from very small-scale internal structures.

At the resolution of GALFA-H I, as shown in Figure 12, a molecular cloud traced by the $^{12}\text{CO}(J=1-0)$ line appears to be velocity dispersed within a single CNM component. If the observed velocity structure reflects the spatial distribution along the line of sight, the molecular cloud would likewise be interpreted as spatially dispersed. However, this apparent configuration can alternatively be understood as an ensemble of numerous small-scale CNM and molecular cloudlets that remain unresolved in the present observations, as illustrated in Figure 12(b). These fine CNM structures are estimated to have characteristic sizes smaller than ~ 0.2 pc, below the spatial resolution limit of GALFA-H I. If only a subset of these small CNM clumps undergo molecular cloud formation, low resolution observations would exhibit an apparent velocity offset between the CNM and molecular cloud peaks. As noted earlier, although the velocity resolution of GALFA-H I is sufficiently high to resolve the intrinsic CNM line width, its spatial resolution is too coarse to resolve such fine internal structures. It should be noted, however, that the CO structures analyzed in this study may also be spatially smoothed by the telescope beam, implying that even smaller molecular substructures could be embedded within the CNM and remain unresolved.

From Figure 9, the CNM line width is on the order of several km s^{-1} . However, the sound speed within the CNM cloud, given by $c_s = \sqrt{k_B T / \mu m_H}$, is $\sim 1 \text{ km s}^{-1}$. For a kinetic temperature of 100 K, the non-thermal component of the line width in many cases exceeds 1 km s^{-1} . If this supersonic non-thermal broadening is interpreted as bulk gas motion within the CNM, dissipation through shock waves would prevent the maintenance of such motion over long timescales. Alternatively, if multiple small CNM structures overlap along the line of sight and move collectively, their surroundings would be filled with WNM or LNM at higher temperatures (with sound speeds of $\sim 10 \text{ km s}^{-1}$). In this case, the relative motion of the small CNM clouds would be subsonic with respect to the surrounding medium, and shock dissipation would not occur. Consequently, the observed supersonic velocity dispersion could be sustained over extended periods.

This interpretation is supported by theoretical studies (e.g., Koyama & Inutsuka 2002; Audit & Hennebelle 2005; Heitsch et al. 2005), which demonstrate that the CNM develops sub pc scale filamentary or clumpy structures through thermal instability. These simulations indicate that internal velocity dispersions within individual CNM clumps remain subsonic, while relative velocities between clumps typically reach $2 - 5 \text{ km s}^{-1}$.

If molecular clouds are formed from such small CNM clumps, their motions are expected to be inherited by the resulting molecular clouds. Observational studies have indeed reported small scale structures in the interstellar medium. Sakamoto (2002) and Sakamoto & Sunada (2003) identified $\sim 10,000$ au scale substructures at the edges of high latitude clouds (MBM 54 and MBM 55), and in the Heiles Cloud 2 region in Taurus. Tachihara et al. (2012) detected small cloudlets with low internal velocity dispersions but inter-cloud dispersions of several km s^{-1} on scales of $1,000-10,000$ au from $^{12}\text{CO}(J=1-0)$ and $3-2$ observations in the LDN 204 molecular cloud interacting with an H II region, suggesting that such cloudlets may be the origin of non thermal line

broadening. However, it remains unclear whether these structures originate from the CNM. Therefore, future high-resolution, combined H I and CO observations are required to test this hypothesis.

6 Summary

Using ROHSA, we decomposed the GALFA-HI data of the molecular cloud formation region HLCG 92–35, observed with the Arecibo Telescope, into three phases: the Warm Neutral Medium (WNM), Lukewarm Neutral Medium (LNM), and Cold Neutral Medium (CNM). Nine Gaussian components were employed for the spectral decomposition, consisting of two for the WNM, one for the LNM, and six for the CNM. Furthermore, Astrodendro was applied to identify clump-like structures within the CNM and to derive their physical parameters. For comparison with the CNM, we used $^{12}\text{CO}(J=1-0)$ data obtained with the NANTEN telescope.

These analyses reveal that the observed CNM structures are broadly consistent with the picture suggested by previous theoretical studies. In particular, the indications of sub pc scale structure emphasize the importance of future high-resolution H I/CO observations.

Our main findings are summarized as follows:

1. An inverse correlation was found between the CNM and LNM distributions, with small-scale CNM structures embedded within the extended LNM envelope. This morphology closely resembles the locally enhanced CNM regions reported by Kalberla & Haud (2018), suggesting that such environments are conducive to molecular cloud formation.
2. In the HLCG 92–35 region, the H I mass ratio among the three phases was determined to be CNM:LNM:WNM = 43:47:10, indicating a clear predominance of LNM. This result implies that the gas has been driven out of thermal equilibrium by turbulence, and that the thermodynamic state of H I may still be governed by residual energy input from past shock-driven processes.
3. A total of 2,214 CNM clumps were identified by Astrodendro, with an average size of 0.4 pc and an average density of $\sim 101 \text{ cm}^{-3}$. These sub-parsec, high-density structures are consistent with predictions from theoretical simulations. While most CNM clumps are relatively diffuse, a subset of high-density clumps likely represents the earliest stages of molecular cloud formation.
4. The mass spectrum of CNM clumps follows a power law of $dN/dM \propto M^{-1.92}$ for $0.05 < M < 0.5 M_\odot$, but steepens significantly at higher masses. CO clumps ($M > 0.5 M_\odot$) exhibit a power-law slope of $M^{-1.86 \pm 0.06}$, which is consistent with that of the intermediate-mass CNM. This similarity in the mass distributions suggest that molecular clouds inherit the hierarchical structure of the CNM. This result implies that the self-similar nature of the gas is maintained throughout the evolutionary transition from atomic to molecular phases, likely governed by thermal instability and turbulent compression.
5. Analysis of CNM linewidths revealed a substantial non-thermal component. The velocity offsets between CNM and CO (typically $0.5-1 \text{ km s}^{-1}$) appear to be local phenomena arising from structural inhomogeneities within the CNM. These features imply that the CNM may consist of unresolved, subsonic small scale clouds moving collectively as aggregates potentially representing the earliest phase of molecular cloud formation.

Acknowledgements

This publication utilizes data from Galactic ALFA HI (GALFA-HI) survey data set obtained with the Arecibo L-band Feed Array (ALFA) on the Arecibo 305m telescope. The Arecibo Observatory is a facility of the National Science Foundation (NSF) operated by SRI International in alliance with the Universities Space Research Association (USRA) and UMET under a cooperative agreement. The GALFA-HI surveys are funded by the NSF through grants to Columbia University, the University of Wisconsin, and the University of California. The NANTEN telescope was operated under a mutual agreement between Nagoya University and the Carnegie Institution of Washington, with additional support from Japanese public donors and companies. This work was financially supported by JST SPRING, Grant Number JPMJSP2125. The author Y.M. would like to thank the “THERS Make New Standards Program for the Next Generation Researchers.”

Appendix 1 Supplementary Maps of HI Components and HI/CO Clumps

Figure 13 shows the integrated intensity maps of the nine HI components separated using ROHSA. The color scale differs for each component. For the six CNM phases, Figure 14 presents the CNM clump structures identified in each component, overlaid on their corresponding parent integrated intensity maps. Figure 15 shows the CO clumps in the HLCG 92–35 region identified using Astrodendro. The clump identification was performed on the entire $^{12}\text{CO}(J=1-0)$ data set; however, only the clumps located within the HLCG 92–35 region shown in Figure 16 were used for the analysis. Clumps lying on or near the boundary of the analyzed region were excluded, and only the clumps marked by plus symbols were included. In this figure, the CNM clump structures are overlaid as contours on the $^{12}\text{CO}(J=1-0)$ integrated intensity map, with plus symbols indicating the clump centroids.

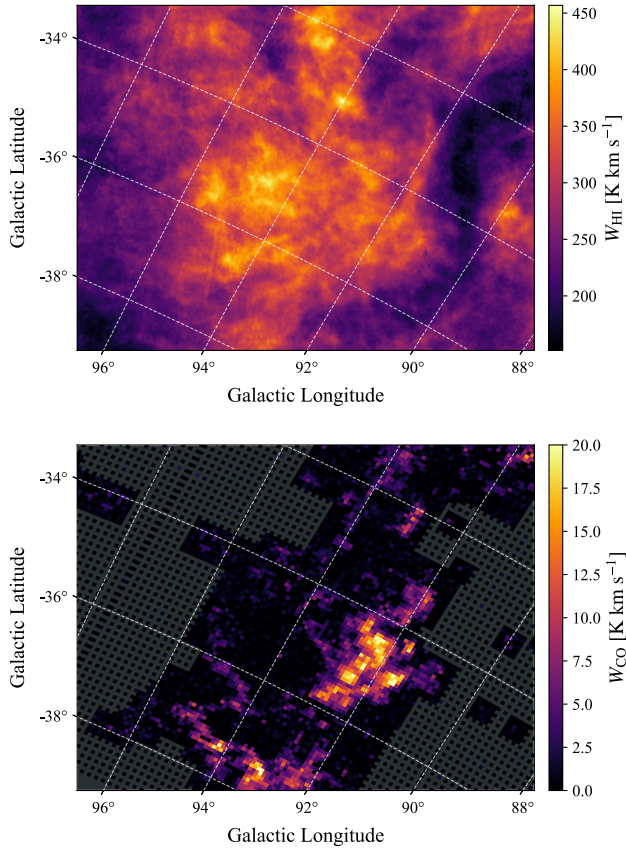


Fig. 1. (Top) Integrated intensity map of the H I emission line in the HLCG 92°-35 region, integrated over the velocity range $-95.5 \text{ km s}^{-1} \leq v_{\text{LSR}} \leq 69.1 \text{ km s}^{-1}$. (Bottom) Integrated intensity map of the $^{12}\text{CO}(J=1-0)$ emission line in the same region, integrated over $-20 \text{ km s}^{-1} \leq v_{\text{LSR}} \leq 10 \text{ km s}^{-1}$. Gray indicates regions outside the observing area. Alt text: Two Galactic coordinate maps of the HLCG 92°-35 region. The top panel shows integrated neutral hydrogen intensity and the bottom panel shows integrated CO intensity. Unobserved areas are masked.

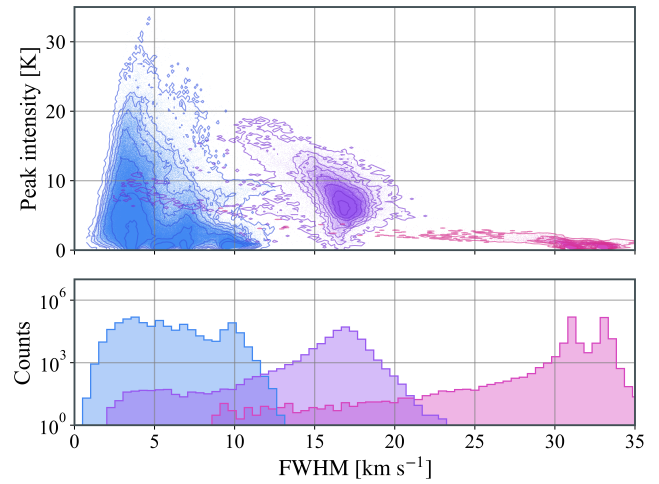


Fig. 2. (Top) Distribution of 1,575,000 Gaussian components decomposed by ROHSA in the FWHM–peak intensity plane. Colors indicate the phase classification: CNM (blue), LNM (purple), and WNM (red). Contours represent the point density. (Bottom) Histogram of the Gaussian FWHM values for each phase, with the vertical axis shown on a logarithmic scale. The FWHM distributions are not completely separated by phase and exhibit partial overlap between the components. Alt text: Two vertically stacked panels showing properties of Gaussian components derived from neutral hydrogen data. The top panel presents peak intensity as a function of full width at half maximum for one hundred fifty five thousand components. The bottom panel shows the distribution of full width at half maximum values as a histogram on a logarithmic count scale.

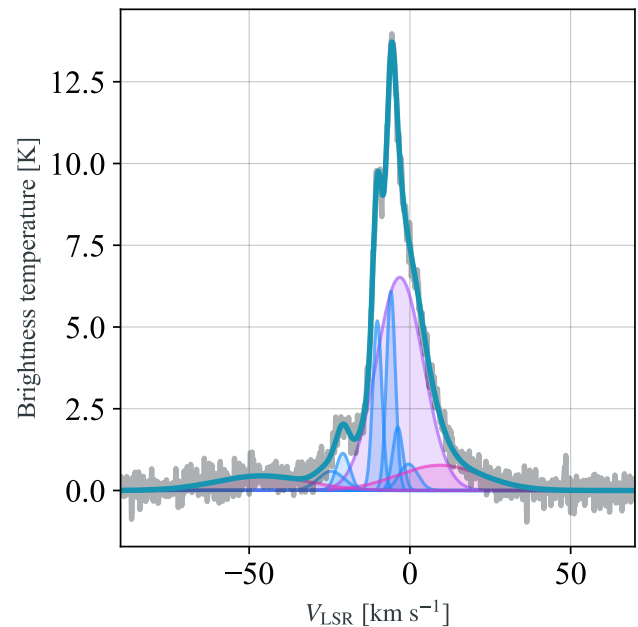


Fig. 3. Example of multi-Gaussian fitting using ROHSA. The gray line represents the original spectral data, while the red, purple, and blue lines correspond to the WNM, LNM, and CNM components, respectively. The green line indicates the sum of all fitted components. Alt text: Multi Gaussian fit to a neutral hydrogen spectrum. Brightness temperature is shown as a function of velocity with respect to the local standard of rest. Components correspond to cold, lukewarm, and warm neutral media, and their sum matches the observed profile.

Table 1. r.m.s ratios for 60 different parameter combinations. The horizontal axis represents the regularization parameters ($\lambda_a, \lambda_\mu, \lambda_\sigma$) and λ'_σ , while the vertical axis indicates the number of Gaussians used. r.m.s ratios close to 1 indicate higher fitting accuracy. In this study, the parameter set $(N, \lambda_a, \lambda_\mu, \lambda_\sigma, \lambda'_\sigma) = (9, 10, 10, 10, 1)$ yielded the best performance.

$N = 6$	0.783	0.804	0.807	0.789	0.719	0.735	0.749	0.737	0.664	0.644	0.685	0.674
7	0.829	0.834	0.844	0.835	0.78	0.793	0.795	0.797	0.756	0.76	0.758	0.74
8	0.896	0.899	0.895	0.878	0.806	0.82	0.854	0.843	0.819	0.798	0.805	0.786
9	0.916	0.921	0.919	0.899	0.88	0.888	0.886	0.864	0.847	0.849	0.837	0.828
10	0.878	0.884	0.893	0.892	0.844	0.848	0.863	0.863	0.828	0.836	0.833	0.828
$\lambda_a, \lambda_\mu, \lambda_\sigma$	1	10	100	1000	1	10	100	1000	1	10	100	1000
λ'_σ	1	1	1	1	10	10	10	10	100	100	100	100

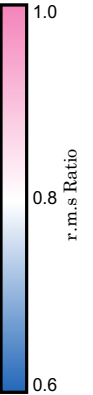


Table 2. Average peak intensity and velocity dispersion σ of the nine components ($G_1 - G_9$) separated by ROHSA in the HLCG 92 \sim 35 region.

Component	G_1	G_2	G_3	G_4	G_5	G_6	G_7	G_8	G_9
peak intensity [K]	7.3	6.8	3.4	4.7	7.1	1.2	0.4	1.3	0.4
velocity dispersion σ [km s $^{-1}$]	7.1	1.5	2.9	1.6	1.6	4.0	13.1	2.3	14.0

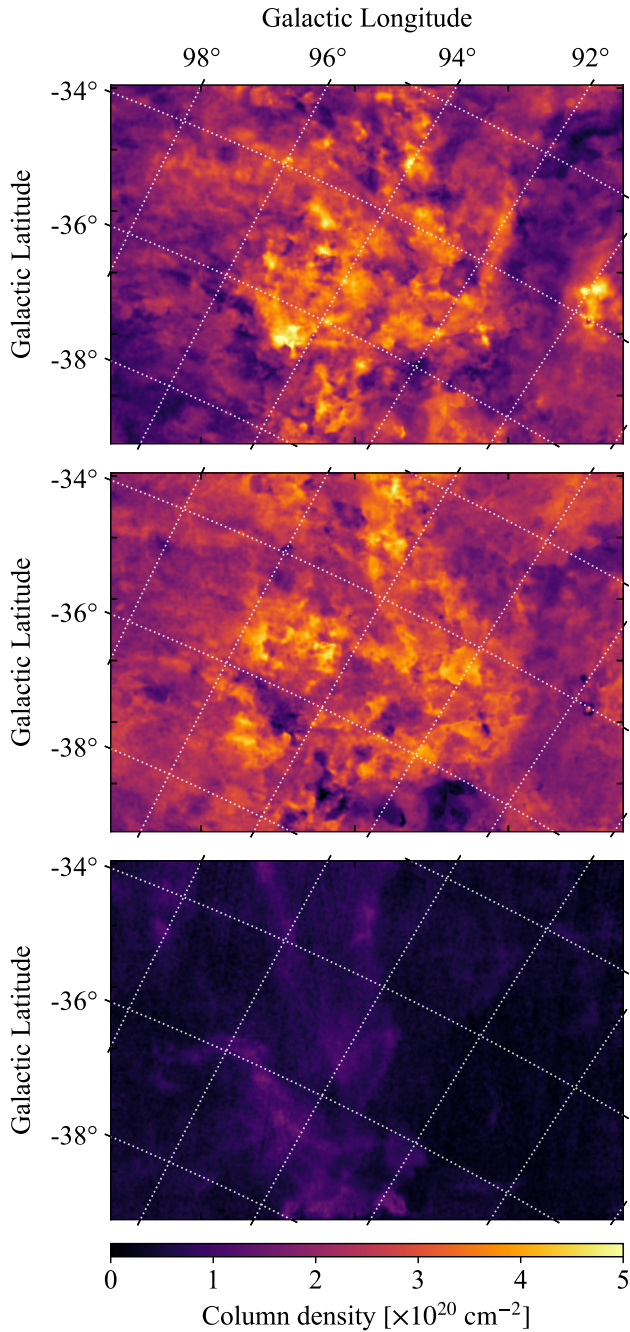


Fig. 4. Column density maps of H I phases. (Top) CNM, (Middle) LNM, and (Bottom) WNM. The spatial domain is the same as in Figure 1. Alt text: Three Galactic coordinate maps showing neutral hydrogen column density separated by phase. The top, middle, and bottom panels correspond to cold neutral medium, lukewarm neutral medium, and warm neutral medium, respectively.

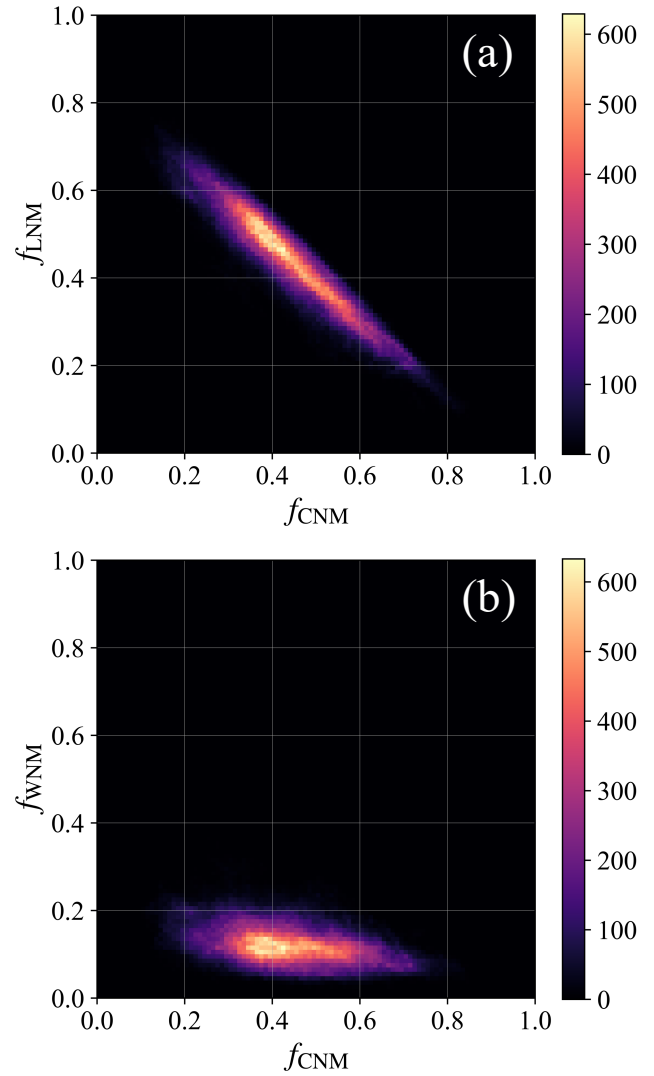


Fig. 5. Two-dimensional frequency distribution of mass fraction in the HLCG 92–35 region. (a) Frequency distribution of f_{WNM} and f_{LNM} , (b) Frequency distribution of f_{LNM} and f_{CNM} . Alt text: Two vertically stacked density plots showing the frequency distribution of neutral hydrogen mass fractions in the HLCG 92–35 region. Panel a presents the mass fraction of warm neutral medium versus cold neutral medium. Panel b presents the mass fraction of lukewarm neutral medium versus cold neutral medium.

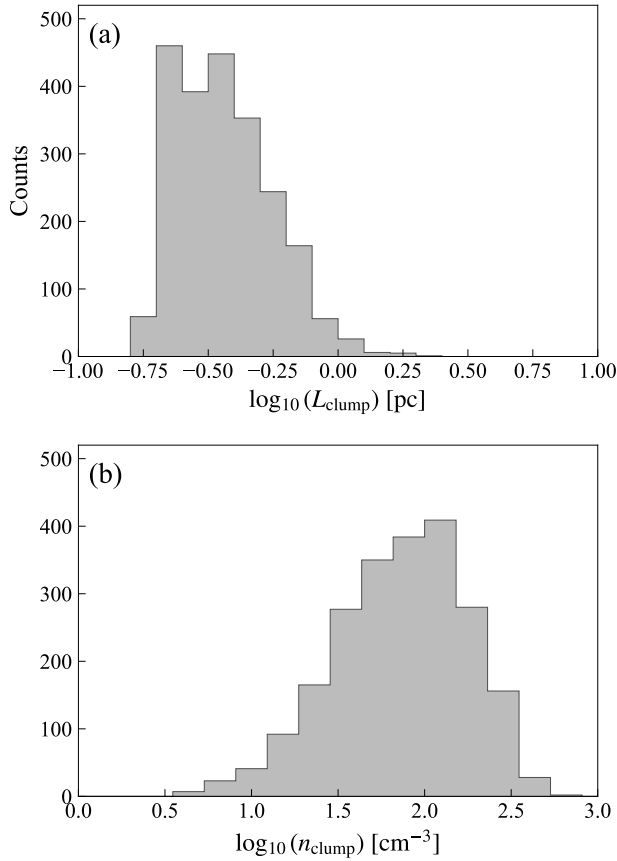


Fig. 6. (a) Size histogram of CNM clumps. (b) Number density histogram of cold neutral medium CNM clumps. Alt text: Two histograms showing statistical distributions of cold neutral medium clumps. The upper panel presents the logarithm of effective radius in parsecs, and the lower panel shows the logarithm of number density in cubic centimeters. The vertical axis in both panels represents counts.

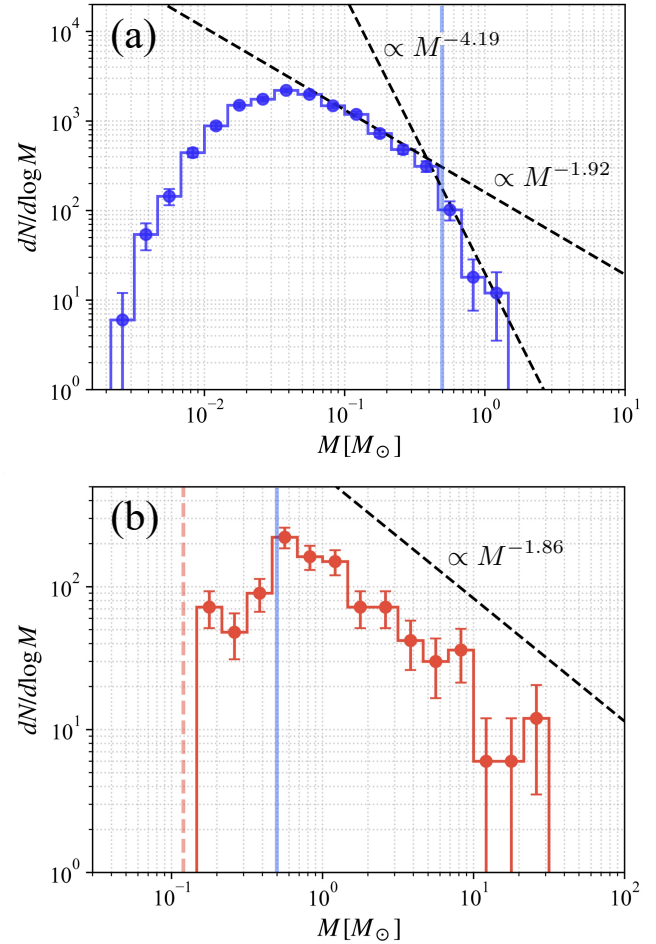


Fig. 7. (a) CNM mass spectrum. The lines indicate reference slopes of $dN/dM \propto M^{-1.92}$ and $\propto M^{-4.19}$. The CNM clump distribution deviates from the -1.92 power law at both the low-mass and high-mass ends. (b) CO clump mass spectrum (red). The CNM clump mass spectrum from Figure 7(a) is shown in blue for comparison. The solid line indicates a reference slope of $dN/dM \propto M^{-1.86}$, and the red dashed line represents the CO clump detection limit. The blue vertical line indicates $0.5M_{\odot}$ and is the same in (a) and (b). Alt text: Two panels displaying mass spectra of cold neutral medium and carbon monoxide clumps. The horizontal axis shows mass in solar masses, and the vertical axis shows number per logarithmic mass interval, both on logarithmic scales.

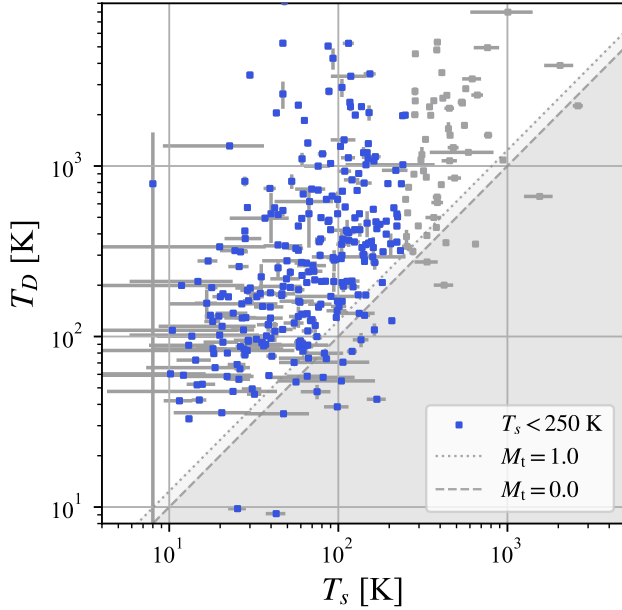


Fig. 8. Distribution of spin temperature (T_s) and Doppler temperature (T_D) of HI components from previous absorption line observations. Components with $T_s < 250$ K, corresponding to the CNM temperature range, are shown in blue. The dotted line indicates $M_t = 1.0$, and the dashed line indicates $M_t = 0.0$. Most components have $M_t > 1$, suggesting that they are in a supersonic state. Alt text: Scatter plot showing the distribution of spin temperature and Doppler temperature of cold neutral medium components. Both axes are logarithmic and expressed in kelvin. Data points are plotted with reference lines indicating constant Mach numbers.

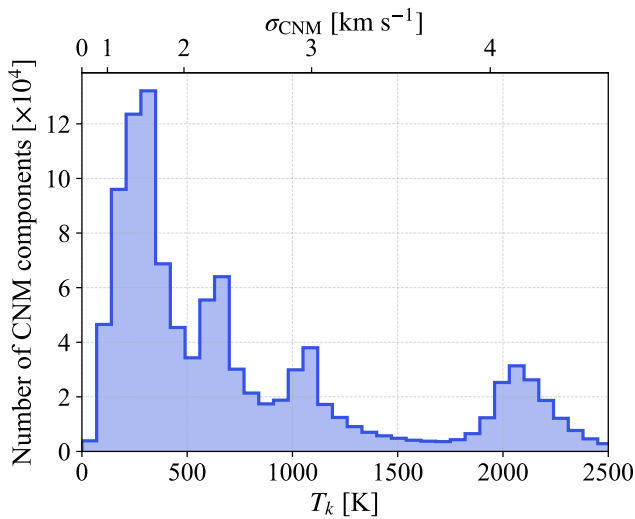


Fig. 9. Distribution of line widths for all CNM components separated by ROHSA, converted to temperature. The corresponding velocity dispersion (σ) is shown on the upper axis. Alt text: Histogram showing the distribution of line widths of cold neutral medium components separated by ROHSA. The lower axis gives temperature in kelvin converted from line width, and the upper axis shows the corresponding velocity dispersion in kilometers per second. The vertical axis represents the number of components.

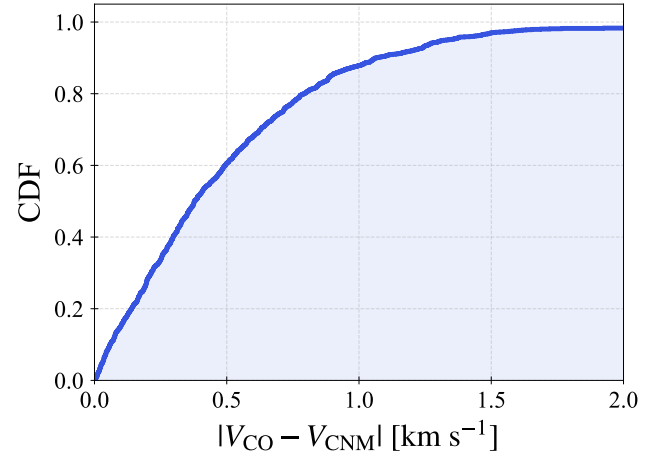


Fig. 10. Cumulative distribution of the absolute velocity difference between CNM and ^{12}CO . The velocity difference is measured between each CO emission line and the CNM component closest to its central velocity. Only lines of sight where the CO peak intensity exceeds 2.0 K ($> 4\sigma$) are shown. Alt text: Cumulative distribution function of the absolute velocity difference between cold neutral medium and CO emission components. The horizontal axis shows velocity difference in kilometers per second, and the vertical axis shows cumulative fraction.

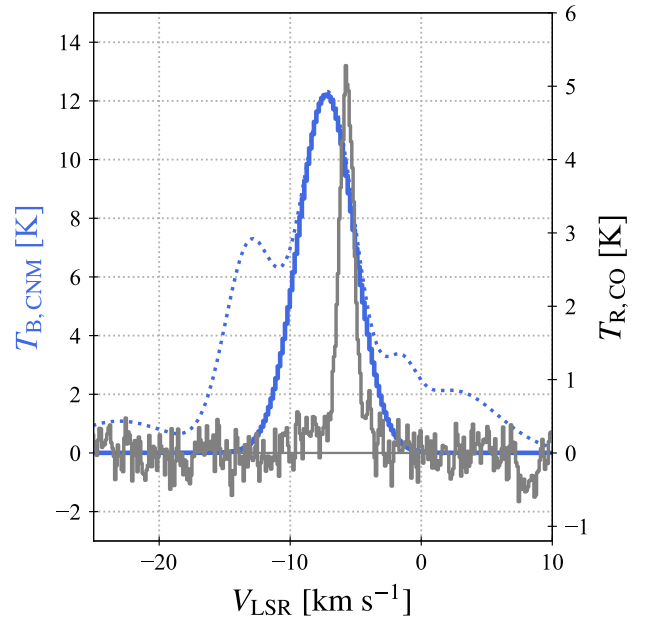


Fig. 11. Velocity offset at $(l, b) = (92.9^\circ, -34.7^\circ)$. The blue spectrum represents the CNM (dashed lines indicate all CNM components), and the gray spectrum represents $^{12}\text{CO}(J = 1-0)$. Alt text: Velocity spectra at Galactic longitude ninety two point nine degrees and latitude minus thirty four point seven degrees. The horizontal axis shows local standard of rest velocity in kilometers per second. The vertical axes show brightness temperature in kelvin for cold neutral medium and carbon monoxide emission. Two spectra are overlaid for comparison.

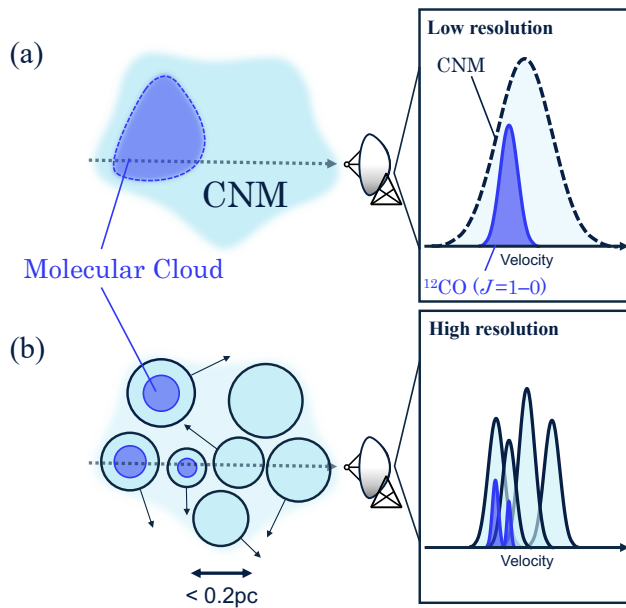


Fig. 12. Schematic illustration of line-width broadening. (a) CNM (light blue) and molecular clouds (dark blue) as seen in low-resolution observations, corresponding to the data used in this study. Within a single CNM, the molecular cloud ($^{12}\text{CO}(J = 1-0)$) appears velocity-dispersed, which would be interpreted as a spatially extended molecular cloud. (b) Actual structure as revealed by high-resolution observations. Both CNM and molecular clouds exhibit sub-0.1 pc fine structures, and the CNM/CO spectra are resolved into multiple narrow-line components. Alt text: Schematic illustration of line width broadening in cold neutral medium and molecular clouds. Panel a shows a large scale structure where a single line of sight produces a broad velocity profile. Panel b shows high resolution observations resolving sub parsec structures into multiple narrow velocity components. Spectral profiles are displayed alongside each schematic.

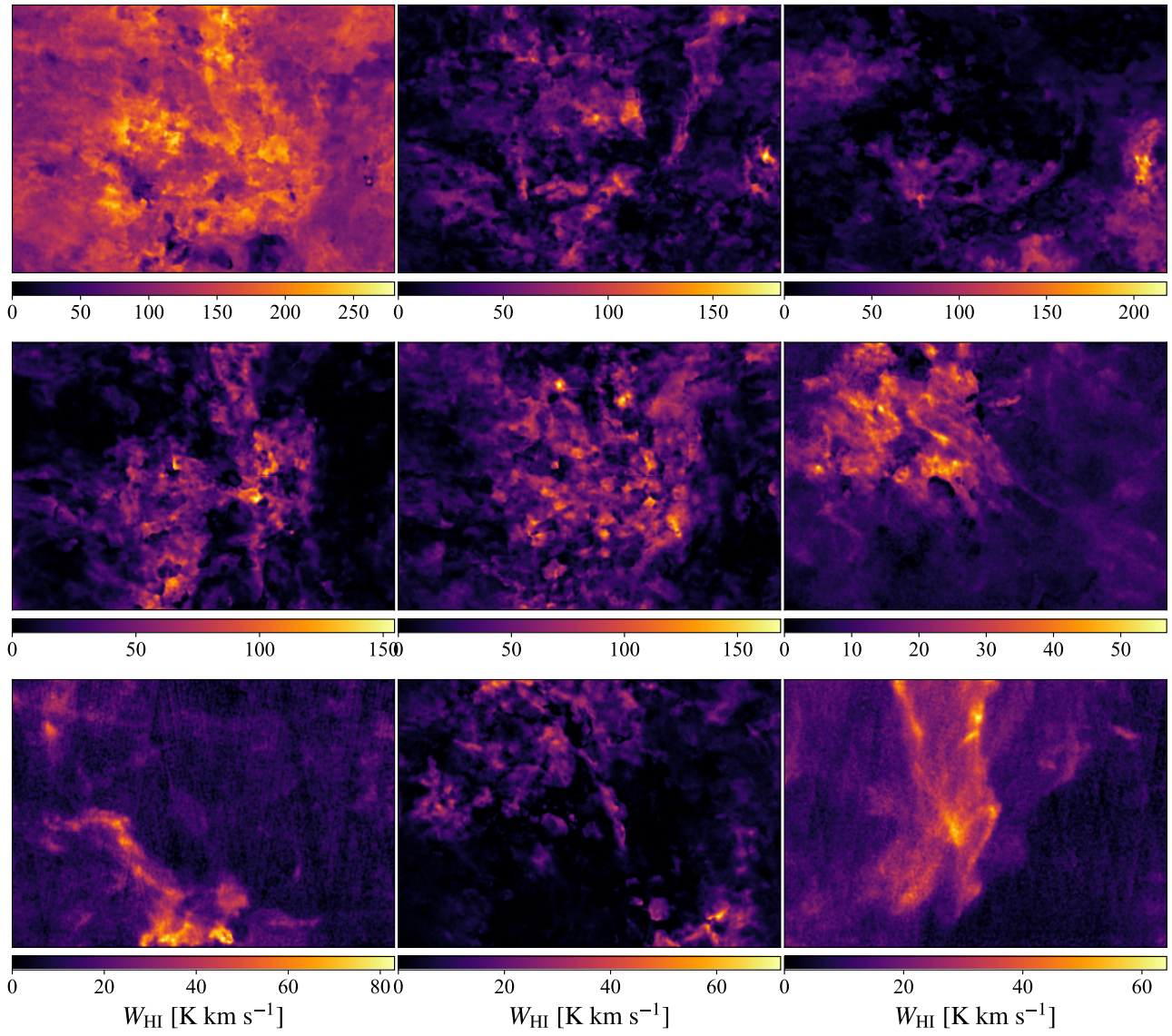


Fig. 13. Integral intensity maps of the nine HI components in the HLCG 92–35 region isolated by ROHSA (left column: G_1, G_4, G_7 ; center: G_2, G_5, G_8 ; right: G_3, G_6, G_9). The displayed region is the same as in Figure 1. The color bar scale varies by map. Coordinates are the same as in Figure 1. Alt text: Nine integrated intensity maps of neutral hydrogen components separated by ROHSA in the HLCG 92–35 region.

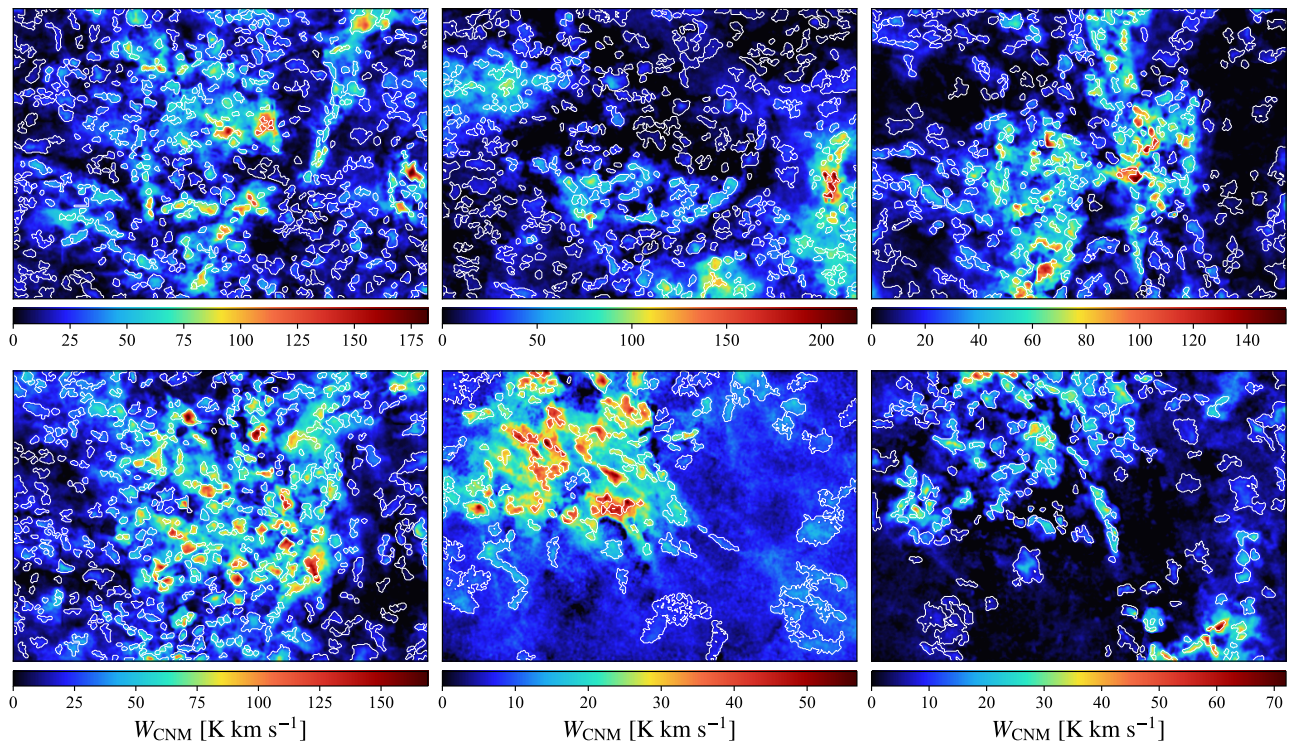


Fig. 14. CNM clumps in the HLCG 92–35 region identified with Astrodendro. Clump structures are shown as contours over the integrated intensity map of six CNM components. Left column: G_2 and G_5 ; center column: G_3 and G_6 ; right column: G_4 and G_8 . Alt text: Spatial distribution of cold neutral medium clumps identified with Astrodendro in the HLCG 92–35 region.

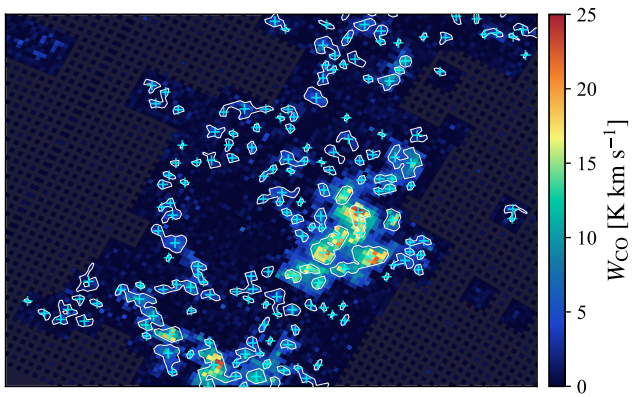


Fig. 15. CO clumps in the HLCG 92–35 region identified with Astrodendro. CO clump structures are overlaid as contours on the $^{12}\text{CO}(J = 1-0)$ integrated intensity map. The “+” symbols indicate the clump centroids. The displayed area corresponds to that in Figure 1; clumps with centroids outside the analyzed region were excluded from the analysis. Alt text: Spatial distribution of CO clumps in the HLCG 92–35 region.

References

- Audit, E., & Hennebelle, P. 2005, *A&A*, 433, 1
- Audit, E., & Hennebelle, P. 2010, *A&A*, 511, A76
- Bellomi, E., Godard, B., Hennebelle, P., Valdivia, V., Pineau des Forêts, G., Lesaffre, P., & Pérault, M. 2020, *A&A*, 643, A36
- Buckland-Willis, F., Miville-Deschênes, M. A., Marchal, A., et al. 2025, *A&A*, 693, A239
- Cotten, D. L., & Magnani, L. 2013, *MNRAS*, 436, 1152
- Dame, T. M., Ungerechts, H., Cohen, R. S., de Geus, E. J., Grenier, I. A., May, J., Murphy, D. C., Nyman, L.-A., & Thaddeus, P. 1987, *ApJ*, 322, 706
- Field, G. B. 1965, *ApJ*, 142, 531
- Field, G. B., Goldsmith, D. W., & Habing, H. J. 1969, *ApJL*, 155, L149
- Fukui, Y., Hayakawa, T., Inoue, T., Torii, K., Okamoto, R., Tachihara, K., Onishi, T., & Hayashi, K. 2018, *ApJ*, 860, 33
- Gazol, A., & Kim, J. 2010, *ApJ*, 723, 482
- Gir, B. -Y., Blitz, L., & Magnani, L. 1994, *ApJ*, 434, 162
- Goodman, A. A., Rosolowsky, E. W., Borkin, Michelle A., Foster, Jonathan B., Halle, M., Kauffmann, J., & Pineda, J. E. 2009, *Nature*, 457, 63
- Haud, U. & Kalberla, P. M. W. 2007, *A&A*, 466, 555
- Heiles, C., & Troland, T. H. 2003, *ApJS*, 145, 329
- Heiles, C., & Troland, T. H. 2003, *ApJ*, 586, 1067
- Heithausen, A., Bensch, F., Stutzki, J., Falgarone, E., & Panis, J. F. 1998, *A&A*, 331, L65
- Heitsch, F., Burkert, A., Hartmann, L. W., Slyz, A. D. & Devriendt, J. E. G. 2005, *ApJL*, 633, L113
- Hennebelle, P., & Audit, E. 2007, *A&A*, 465, 431
- HI4PI Collaboration, Ben Bekhti, N., Flöer, L., et al. 2016, *A&A*, 594, A116
- Hu, Y. 2025, *ApJ*, 986, 62
- Inoue, T., & Inutsuka, S. 2012, *ApJ*, 759, 35
- Kalberla, P. M. W. Burton, W. B. and Hartmann, D., Arnal, E. M. Bajaja, E., Morras, R., & Pöppel, W. G. L. 2005, *A&A*, 440, 775
- Kalberla, P. M. W. & Haud, U. 2018, *A&A*, 619, A58
- Kalberla, P. M. W. 2025, *A&A*, 694, L11
- Kim, C. -G., Ostriker, E. C. 2018, *ApJ*, 853, 173
- Kobayashi, M. I. N., Inoue, T., Inutsuka, S., Tomida, K., Iwasaki, K., & Tanaka, K. E. I. 2020, *ApJ*, 905, 95
- Kobayashi, M. I. N., Iwasaki, K., Tomida, K., Inoue, T., Omukai, K., & Tokuda, K. 2023, *ApJ*, 954, 38
- Koyama, H., & Inutsuka, S. 2002, *ApJL*, 564, L97
- Kramer, C., Stutzki, J., Rohrig, R., & Corneliussen, U. 1998, *A&A*, 329, 249
- Kulkarni, S. R., & Fich, M. 1985, *ApJ*, 289, 792
- Lee, M.-Y., Stanimirović, S., Murray, C. E., Heiles, C., & Miller, J. 2015, *ApJ*, 809, 56
- Magnani, L., Blitz, L., & Mundy, L. 1985, *ApJ*, 295, 402
- Marchal, A., Miville-Deschênes, M. -A., Orioux, F., Gac, N., Soussen, C., Lesot, M. -J., d'Allonnes, A. R., & Salomé, Q. 2019, *A&A*, 626, A101
- Marchal, A., Martin, Peter G., Gong, M. 2021, *ApJ*, 921, 11
- Marchal, A., & Miville-Deschênes, M. -A. 2021, *ApJ*, 908, 186
- McClure-Griffiths, N. M., Stanimirović, S., & Rybarczyk, D. R. 2023, *ARA&A*, 61, 19
- McKee, C. F., & Ostriker, J. P. 1977, *ApJ*, 218, 148
- Mohan, R., Dwarakanath, K. S., & Srinivasan, G. 2004, *J. Astrophys. Astron*, 25, 185
- Murray, C. E., Stanimirović, S., Goss, W. M., et al. 2015, *ApJ*, 804, 89
- Murray, C. E., Stanimirović, S., Goss, W. M., Heiles, C., Dickey, J. M., Babler, B., & Kim, C. 2018, *ApJS*, 238, 14
- Nguyen, H., Dawson, J. R., Lee, M.-Y., Murray, C. E., Stanimirović, S., Heiles, C., Miville-Deschênes, M.-A., & Petzler, A. 2019, *ApJ*, 880, 141
- Nguyen, H., McClure-Griffiths, N. M., Dempsey, J., et al. 2024, *MNRAS*, 534, 3478
- Park, Gyueun., Lee, M.-Y., & Bialy, S., et al. 2023, *ApJ*, 955, 145
- Peek, J. E. G., Babler, B. L., Zheng, Y., et al. 2018, *ApJS*, 234, 2
- Rosolowsky, E. W., Pineda, J. E., Kauffmann, J., & Goodman, A. A. 2008, *ApJ*, 679, 1338
- Roy, N., Kanekar, N., Braun, R., & Chengalur, J. N. 2013, *MNRAS*, 436, 2352
- Roy, N., Kanekar, N., & Chengalur, J. N. 2013, *MNRAS*, 436, 2366
- Sakamoto, S. 2002, *ApJ*, 565, 1050
- Sakamoto, S., & Sunada, K. 2003, *ApJ*, 594, 340
- Saury, E., Miville-Deschênes, M.-A., Hennebelle, P., Audit, E., & Schmidt, W. 2014, *A&A*, 567, A16
- Seifried, D., Schmidt, W., Niemeyer, J. C. 2011, *A&A*, 526, A14
- Seifried, D., Haid, S., Walch, S., Borchert, E. M. A., & Bisbas, T. G. 2020, *MNRAS*, 492, 1465
- Seifried, D., Walch, S., Weis, M., Reissl, S., Soler, J. D., Klessen, R. S., & Joshi, P. R. 2020, *MNRAS*, 497, 4196
- Taank, M., Marchal, A., Martin, P. G. & Vujeva, L. 2022, *ApJ*, 937, 81
- Tachihara, K., Saigo, K., Higuchi, A. E., Inoue, T., Inutsuka, S., Hackstein, M., Haas, M., & Mugrauer, M. 2012, *ApJ*, 754, 95
- Tielens, A. G. G. M., & Hollenbach, D. 1985, *ApJ*, 291, 722
- Valdivia, V., Hennebelle, P., Gérin, M., & Lesaffre, P. 2016, *A&A*, 587, A76
- Verschuur, G. L. 1995, *ApJ*, 451, 645
- Welty, D. E., Hobbs, L. M., Blitz, L., & Penprase, B. E. 1989, *ApJ*, 346, 232
- Wolfire, M. G., Hollenbach, D., McKee, C. F. and Tielens, A. G. G. M. and Bakes, & E. L. O. 1995, *ApJ*, 443, 152
- Wolfire, M. G., McKee, C. F., Hollenbach, D., & Tielens, A. G. G. M. 2003, *ApJ*, 587, 278
- Yamamoto, H., Onishi, T., Mizuno, A., & Fukui, Y. 2003, *ApJ*, 592, 217